CHAPTER IV

RESULTS AND DISCUSSIONS

4.1 Introduction

The results of both whole-rock and mineral chemical analyses are displayed in various diagrams in order to consider the chemical relationship among various intrusive rocks in the study area. Moreover, pressure and temperature of emplacement of these intrusive rocks were estimated by Al-in-hornblende barometer (after Schmidt, 1992) and amphibole-plagioclase thermometer (after Holland and Brundy, 1994), respectively. Symbols for rock-forming minerals in this study are those had been recommended by Kretz (1983). Ferrous (Fe^{2+}) concentrations of ferromagnesian minerals were estimated after Droop (1987).

4.2 Whole-rock geochemistry

4.2.1 Major and minor elements

According to major and minor elements, even though both wet chemical and XRF analyses (see Appendix B) yield a non significant different result. Some Harker variation diagrams, which are plotted between major and minor elements against SiO_2 show the conformable trends (Figures 4.1 – 4.5) but wet analysis is more reliable than XRF. This is because its calibration curve was prepared by using USGS rock standards as mentioned in the previous chapter whereas the XRF was analyzed by SemiQ software which is a standardless method. Therefore, major and minor element result obtained by the wet analysis (Table 4.1) are used in this thesis.

4.2.2 Trace elements

The concentration of Ba, Cu, Pb, Zn, Rb and Sr were analysed by AAS while Nb, Y, La, Ce, Pr, Nd, Sm, Eu, Gd and Yb were analysed by ICP-OES. These results are also presented in Table 4.1.

Table 4.1 Major, minor and trace element concentrations of intrusive rocks in the study area.

	Gabbro					Diorite					Hbl-Bt granodiorite					Qtz diorite				
	pn 65	pn 66	pn 68	pn 69	pn 70	pn 22	pn 30	pn 44	pn 50	pn 54	pn 36	pn 37	pn 38	pn 58	pn 59	pn 2	pn 4	pn 6	pn 7	pn 20
SiO2	55.37	51.39	51.94	52.38	55.82	58.16	56.36	56.96	58.51	57.24	66.2	62.99	64.84	61.48	62.66	62.27	62.47	64.06	62.99	61.5
TiO2	1.7	1.15	1.5	1.54	1.52	1.08	1.15	1.28	1.06	1.09	0.74	1.08	0.66	1.01	1.15	0.79	0.71	0.75	0.78	0.93
Al2O3	17.03	18.3	16.05	17.49	17.15	17.18	16.49	17	16.74	17.58	16.04	16.78	15.39	16.11	16.11	15.46	15.21	17.38	15.87	17.51
Tot Fe	7.29	5.05	8.25	8.7	6.79	6.52	7.42	7.11	6.67	6.76	3.47	4.77	3.16	4.65	5.09	5.06	4.07	3.79	5.58	4.59
MgO	5.68	5.57	4.914	5.18	5.04	5.22	5.39	5.56	4.2	5.21	2.7	3.19	2.56	4.01	4.21	5.78	3.59	3.53	5.25	3.8
CaO	7.81	14.32	12.55	10.71	6.78	6.91	8.7	7.25	6.2	7.03	3.74	5.17	3.44	5.29	5.31	4.49	5.94	4.54	4.3	5.3
Na2O	4.17	3.11	3.85	3.55	4.42	3.59	3.78	3.57	4.19	3.96	4.2	4.05	4.03	4.46	4.10	4.32	4.59	4.11	4.24	4.19
K2O	0.78	0.37	0.29	0.69	1.22	1.18	0.71	1.11	1.17	0.53	1.67	1.81	1.31	1.61	1.73	1.33	1.37	1.42	1.25	1.03
P2O5	0.38	0.41	0.23	0.24	0.17	0.08	0.02	0.04	0.36	0.12	0.04	0.36	0.29	0.21	0.23	0.26	0.21	0.14	0.09	0.31
MnO	0.11	0.13	0.15	0.11	0.11	0.12	0.1	0.1	0.14	0.11	0.03	0.07	0.03	0.07	0.07	0.07	0.08	0.08	0.07	0.07
LOI	0.05	0.05	0.36	0.03	0.57	0.17	0.27	0.31	0.27	0.25	0.3	0.1	0.26	0.13	0.11	0.23	0.27	0.29	0.26	0.3
Total	100.37	99.85	100.08	100.62	99.59	100.21	100.39	100.29	99.51	99.88	99.13	100.37	95.97	99.03	100.83	100.06	98.51	100.09	100.68	99.53
Trace and rare earth elements (ppm)																				
Ba*	88.00	73.00	38.00	114.00	137.00	152.00	83.00	142.00	131.00	97.00	192.00	152.00	182.00	161.00	160.00	186.00	175.00	144.00	164.00	122.00
Cu*	41.00	12.00	11.00	71.00	76.00	42.00	42.00	145.00	63.00	37.00	27.00	87.00	97.00	47.00	55.00	16.00	19.00	10.00	18.00	21.00
Pb*	39.00	38.00	39.00	36.00	37.00	32.00	30.00	36.00	31.00	35.00	25.00	25.00	26.00	29.00	28.00	23.00	27.00	27.00	25.00	27.00
Zn*	69.00	45.00	70.00	58.00	72.00	56.00	59.00	67.00	58.00	66.00	24.00	30.00	29.00	52.00	48.00	43.00	47.00	48.00	51.00	50.00
Nb**	65.16	39.93	63.72	47.75	42.53	36.17	50.49	40.15	28.56	n.a	23.44	21.25	21.48	28.41	29.67	23.05	31.85	22.70	41.17	29.12
Rb*	11.00	6.00	1.00	12.00	22.00	16.00	7.00	18.00	16.00	8.00	23.00	29.00	27.00	28.00	29.00	21.00	21.00	21.00	22.00	13.00
Sr*	294.00	346.00	221.00	280.00	250.00	296.00	290.00	364.00	324.00	321.00	194.00	197.00	202.00	232.00	237.00	297.00	242.00	299.00	286.00	361.00
Y**	15.78	16.07	19.39	17.99	17.28	12.14	12.11	16.74	10.56	n.a.	9.19	10.50	8.95	15.04	15.01	9.62	8.95	8.76	8.88	10.83
La**	10.95	8.77	6.47	10.20	12.75	11.12	8.20	11.18	10.47	n.a.	7.08	15.95	15.39	12.37	12.48	11.09	11.10	11.07	11.13	10.91
Ce**	16.28	13.76	10.09	15.49	20.67	16.88	12.75	21.31	16.67	n.a.	8.67	24.55	21.68	19.14	19.86	18.72	16.61	16.75	16.30	16.36
Pr**	13.63	11.29	9.32	12.55	13.64	11.43	12.48	13.64	12.44	n.a.	11.76	13.84	13.78	12.94	13.19	12.42	12.14	12.59	11.99	24.57
Nd**	38.56	32.89	30.12	41.38	37.52	32.56	28.43	35.85	23.89	n.a.	17.81	28.59	27.04	29.43	31.16	23.13	22.34	22.44	22.06	24.57
Sm**	5.11	5.12	4.84	5.71	5.67	4.15	4.13	5.20	4.30	n.a.	3.76	4.36	4.02	5.18	5.60	4.37	3.64	3.97	3.74	4.29
Eu**	1.29	1.20	1.31	1.52	1.27	1.15	1.09	1.28	0.89	n.a.	0.72	0.85	0.79	1.04	1.05	0.78	0.73	0.75	0.76	0.94
Gd**	10.54	8.72	11.82	11.69	9.53	9.05	8.76	10.24	6.81	n.a.	5.41	6.32	5.68	8.07	8.36	5.56	5.74	5.42	5.33	6.54
Yb**	1.83	1.54	2.10	2.14	1.90	1.53	1.43	1.97	1.15	n.a.	1.04	1.17	0.94	1.56	1.63	1.12	0.89	0.91	0.88	1.15

n.a.= not analysed * analysed by AAS ** analysed by ICP-OES

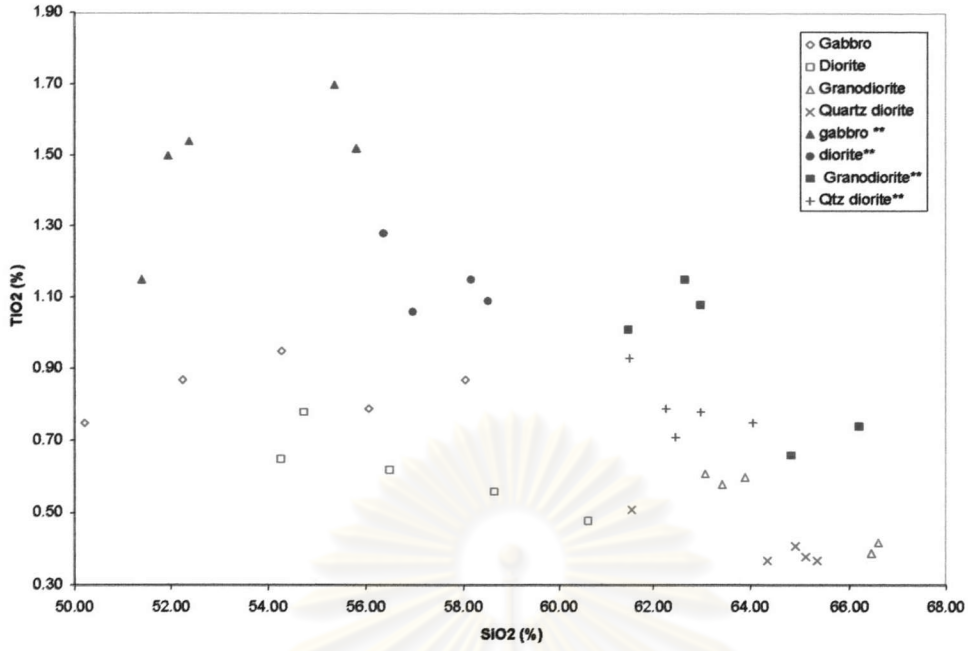

Figure 4.1 Harker variation diagrams of TiO_2 against SiO_2, compare between wet analyses results (solid and cross symbols, blue color) and XRF results (blank symbols, red color).

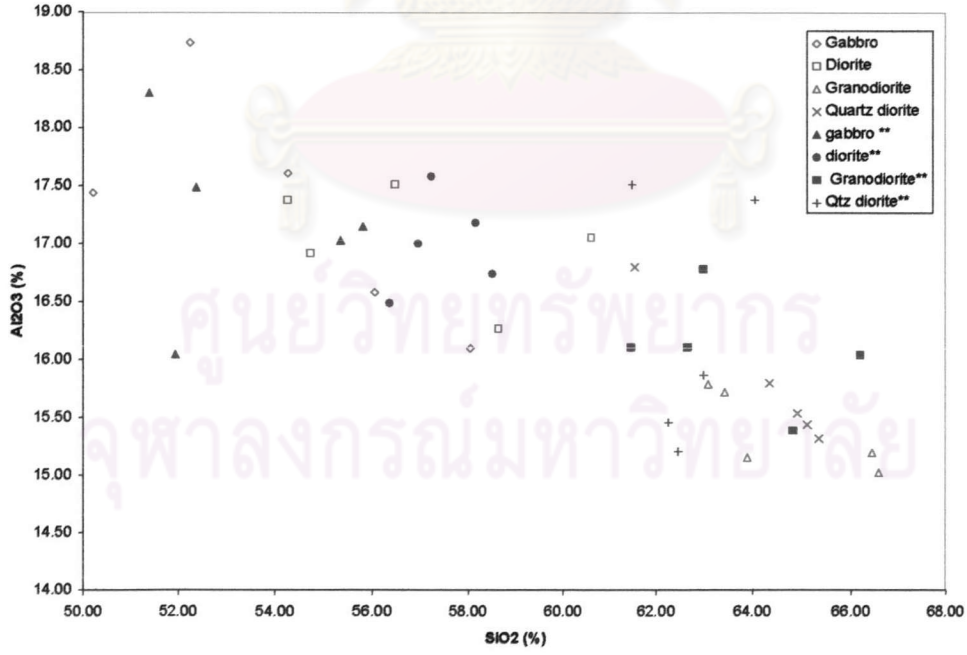

Figure 4.2 Harker variation diagrams of $Al2O_3$ against SiO_2, compare between wet analyses results (solid and cross symbols, blue color) and XRF results (blank symbols, red color).

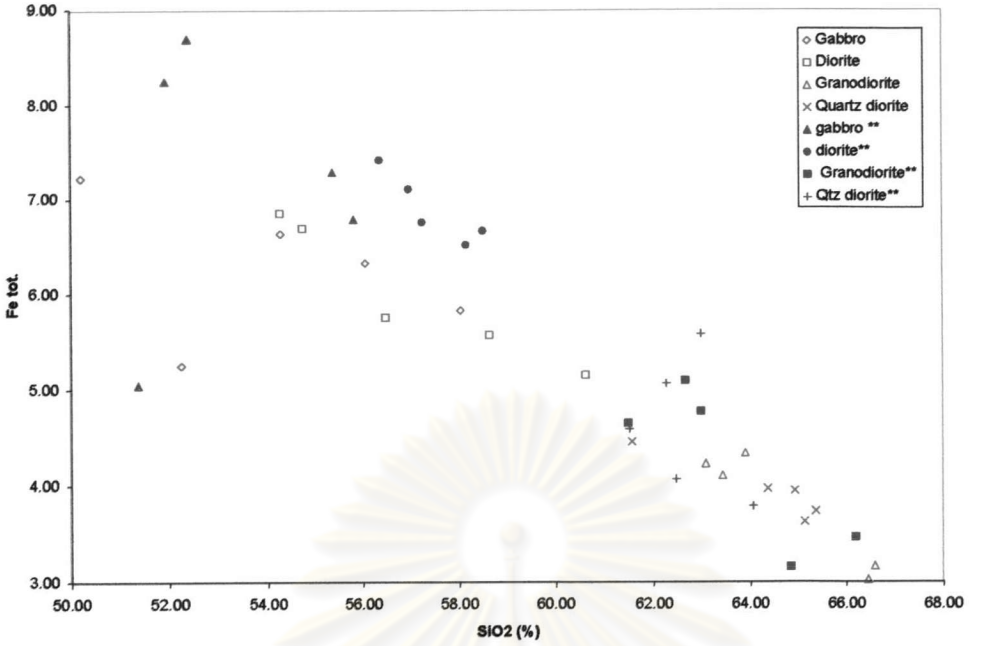

Figure 4.3 Harker variation diagrams of Fe total against SiO_2, compare between wet analyses results (solid and cross symbols, blue color) and XRF results (blank symbols, red color).

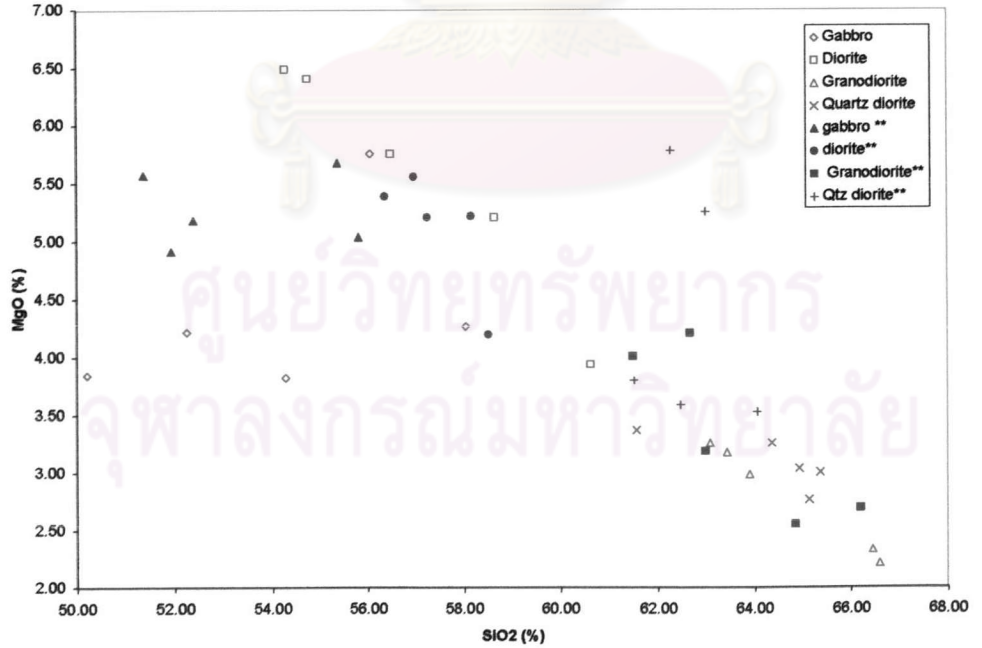

Figure 4.4 Harker variation diagrams of MgO against SiO_2, compare between wet analyses results (solid and cross symbols, blue color) and XRF results (blank symbols, red color).

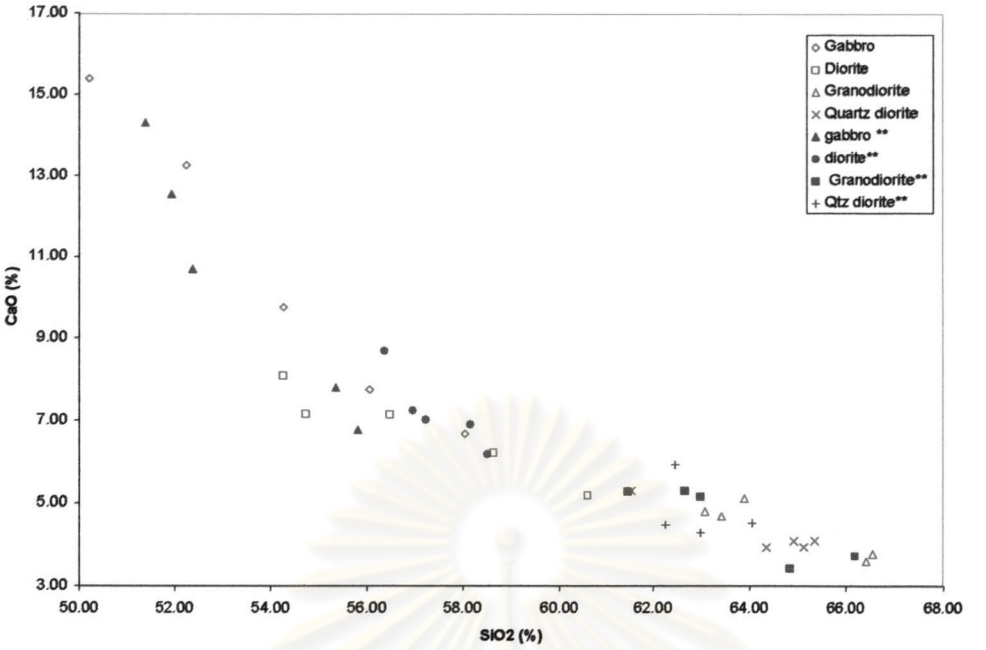

Figure 4.5 Harker variation diagrams of CaO against SiO_2, compare between wet analyses results (solid and cross symbols, blue color) and XRF results (blank symbols, red color).

4.2.3 Rock nomenclature based on major oxides

As mentioned in petrography section, the two finer-grained intrusive rocks, diorite and quartz diorite, were not performed point counting for modal analysis. Therefore, the total alkalis and silica of these two rock types as well as those of the gabbro and hornblende-biotite granodiorite were plotted in the TAS diagram of Wilson (1989) in order to fine out or re-confirm the correct nomenclature of those rocks. As shown in Figure 4.6 the plots of gabbroic rock type fall between mafic to intermediate composition in the fields of gabbro to diorite. Hence the name 'gabbro' is the correct nomenclature for this rock type and it is consistent with the QAP plot of Streckeisen (1976) in Figure 3.34. As for the diorite rock type, the plots fall in the intermediate composition and almost in the diorite field (Figure 4.6). The rock name 'diorite' is therefore the correct nomenclature of this rock type. As for the remaining two rock types they are quite similar in composition from somewhat intermediate to felsic character, and the plots fall in the 'quartz diorite' or 'granodiorite' fields in the TAS diagram. The name 'granodiorite'

is also consistent with the QAP plot of Streckeisen (1976) in Fig. 3.33 Hence all the rock nomenclatures used in this study are correctly named based on the QAP diagram of Streckeisen (1976) as well as the TAS diagram of Wilson (1989).

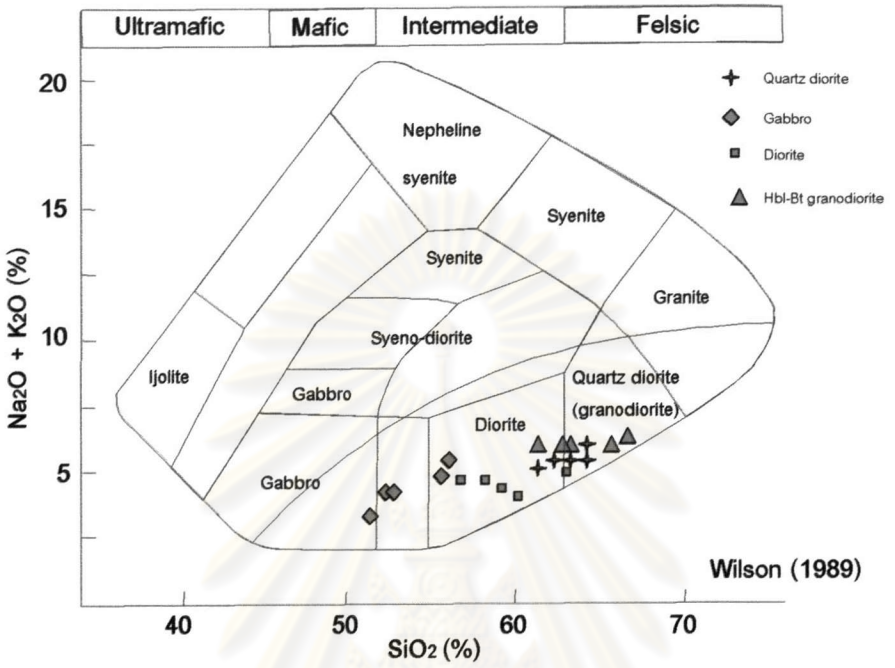

Figure 4.6 Total alkali silica (TAS) diagram.

4.2.4 Chemical variation among various rock types

Plots of each major and minor element or oxide versus SiO_2 content, known as the Harker variation diagrams, are displayed in Figures 4.7 to 4.20. As shown in those plots continuous linear trends of each element increasing or decreasing with respect to increasing of SiO_2 content can be observed. Firstly, TiO_2, Fe_2O_3 (total), MgO, CaO, Al_2O_3, Pb, Nb, MnO, Zn and Y contents decrease corresponding to the increasing SiO_2 content throughout all rock types (Figures 4.7 to 4.16). Secondly, K_2O, Na_2O, Ba and Rb contents show an increasing trend corresponding to an increasing SiO_2 content (Figures 4.17 to 4.20).

All the above diagrams give a reasonable evidence to suggest the same differentiation trend of all rock types in the study area. That means all four intrusive rocks may have a genetic link to one another.

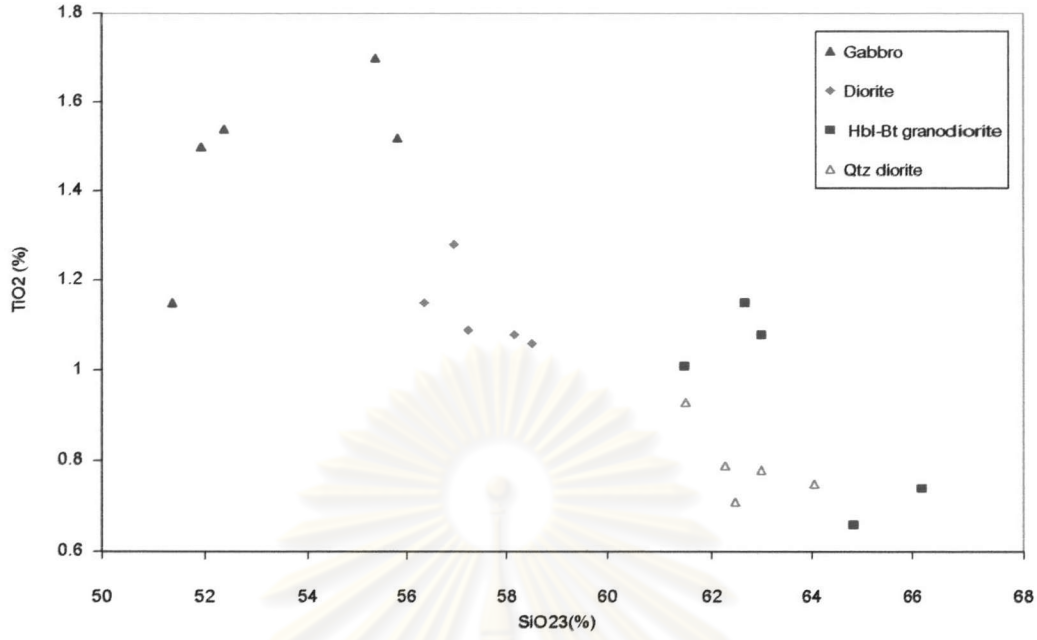

Figure 4.7 Harker variation diagram shows a decreasing of TiO_2 with respect to increasing of SiO_2 content.

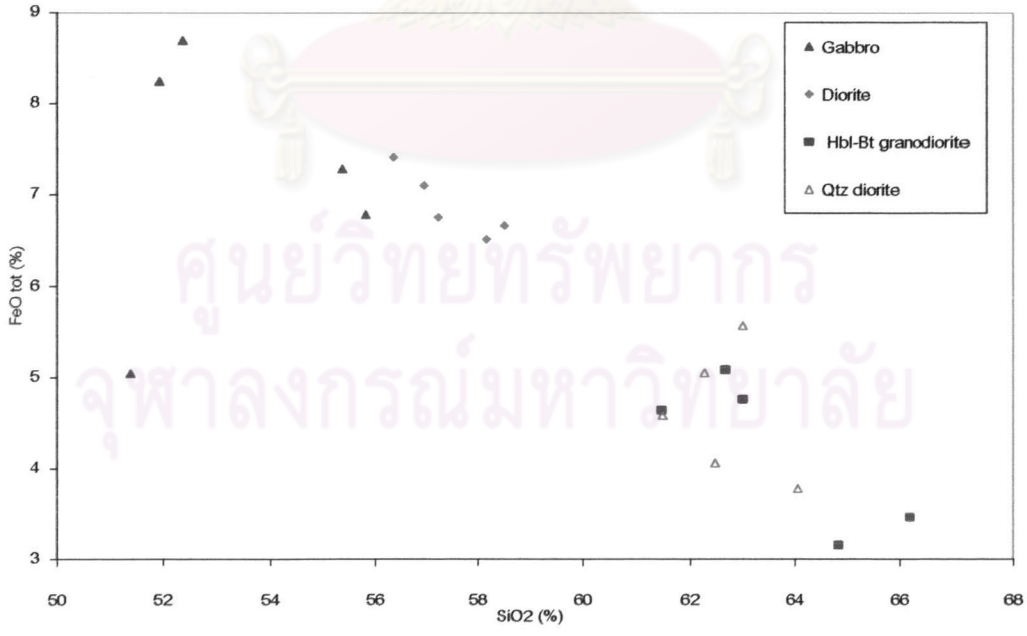

Figure 4.8 Harker variation diagram shows a decreasing of total FeO with respect to increasing of SiO_2 content.

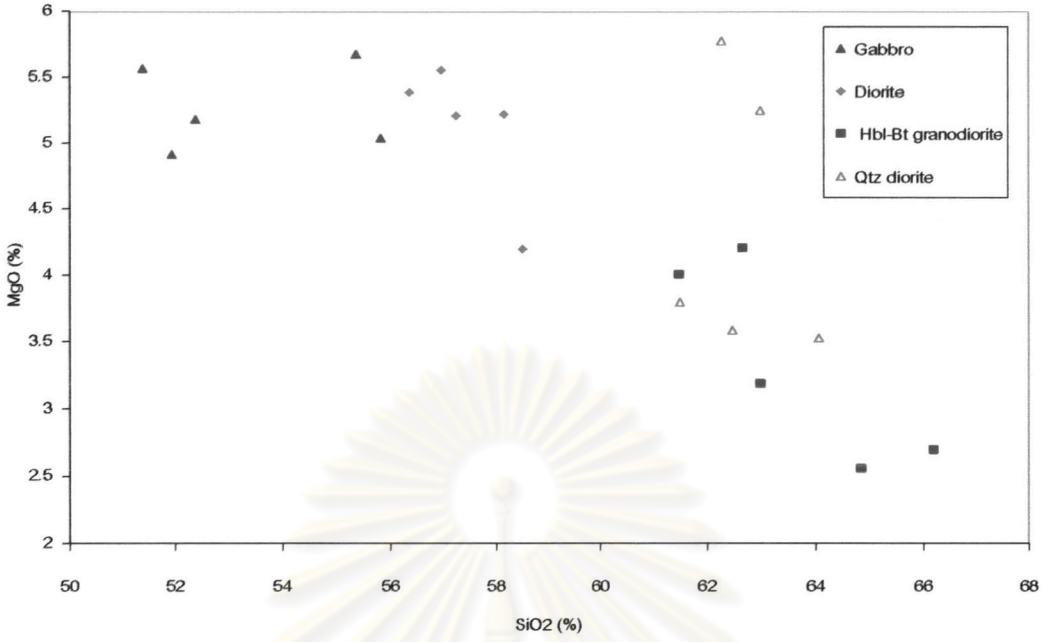

Figure 4.9 Harker variation diagram shows a decreasing of MgO with respect to increasing of SiO_2 content.

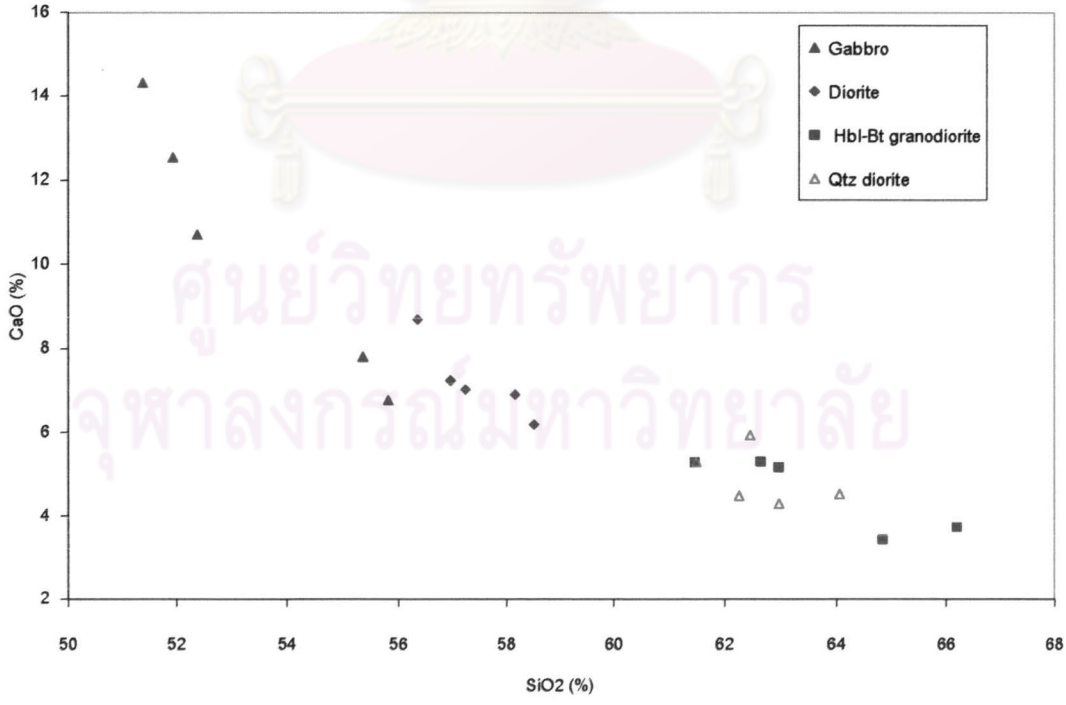

Figure 4.10 Harker variation diagram shows a decreasing of CaO with respect to increasing of SiO_2 content.

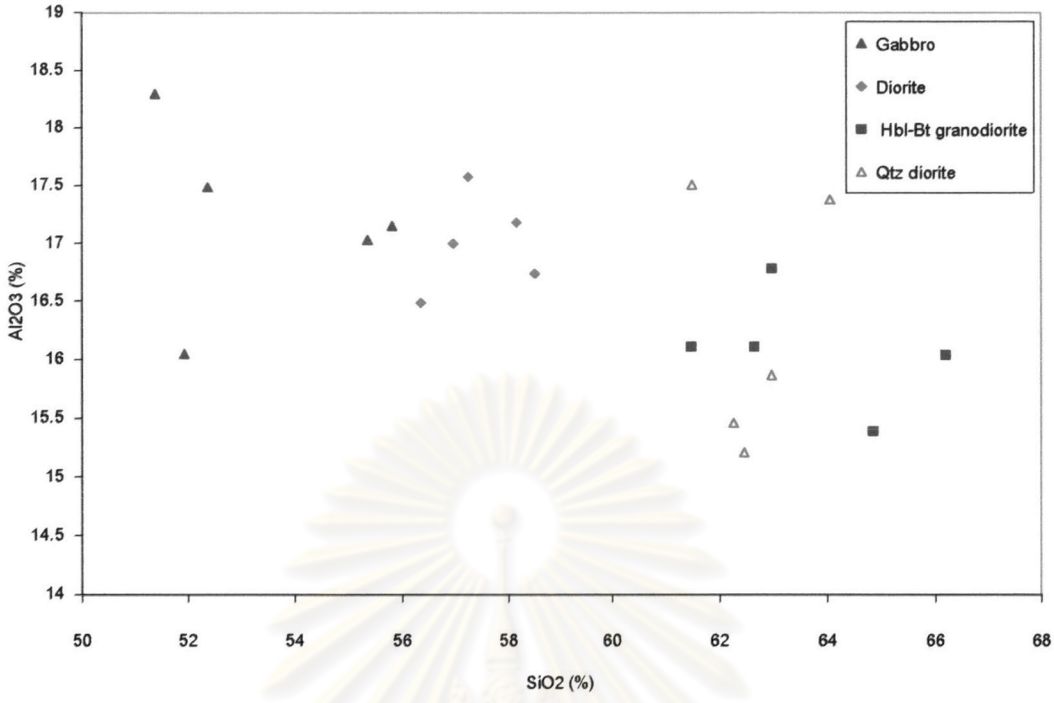

Figure 4.11 Harker variation diagram shows a decreasing of Al_2O_3 with respect to increasing of SiO_2 content.

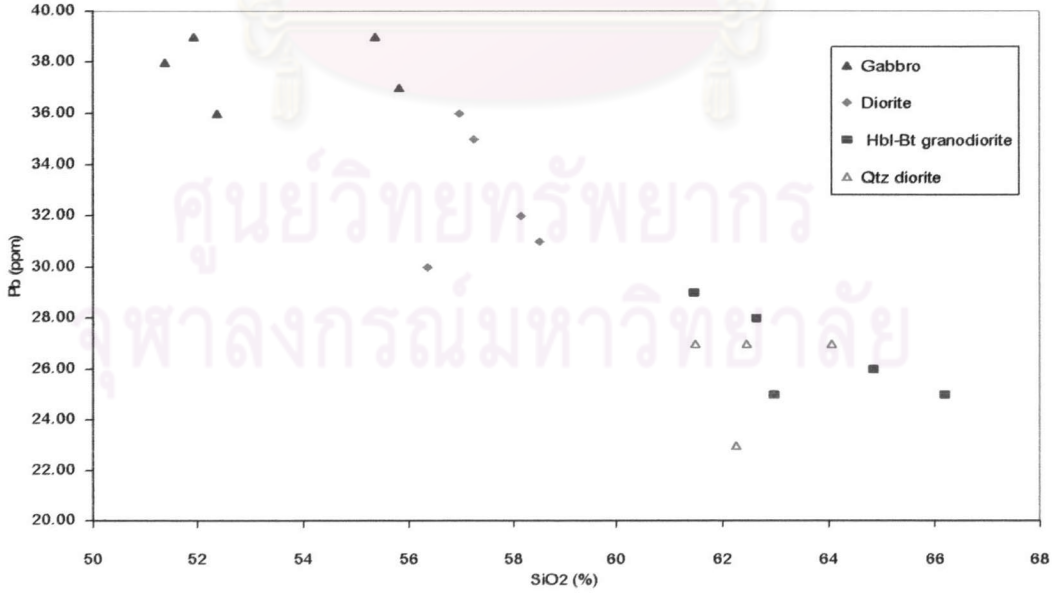

Figure 4.12 Harker variation diagram shows a decreasing of Pb with respect to increasing of SiO_2 content.

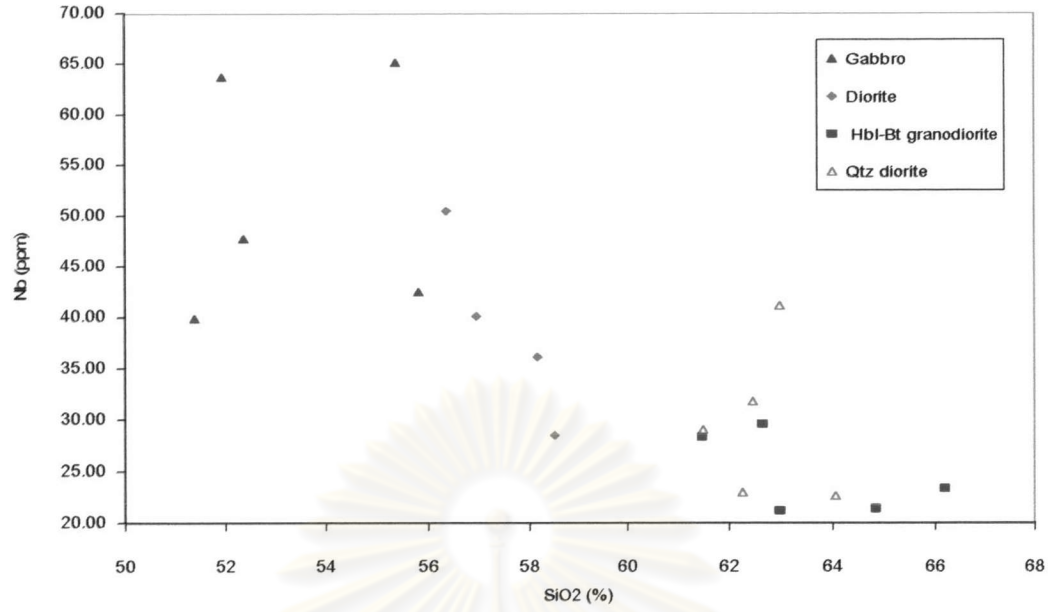

Figure 4.13 Harker variation diagram shows a decreasing of Nb with respect to increasing of SiO_2 content.

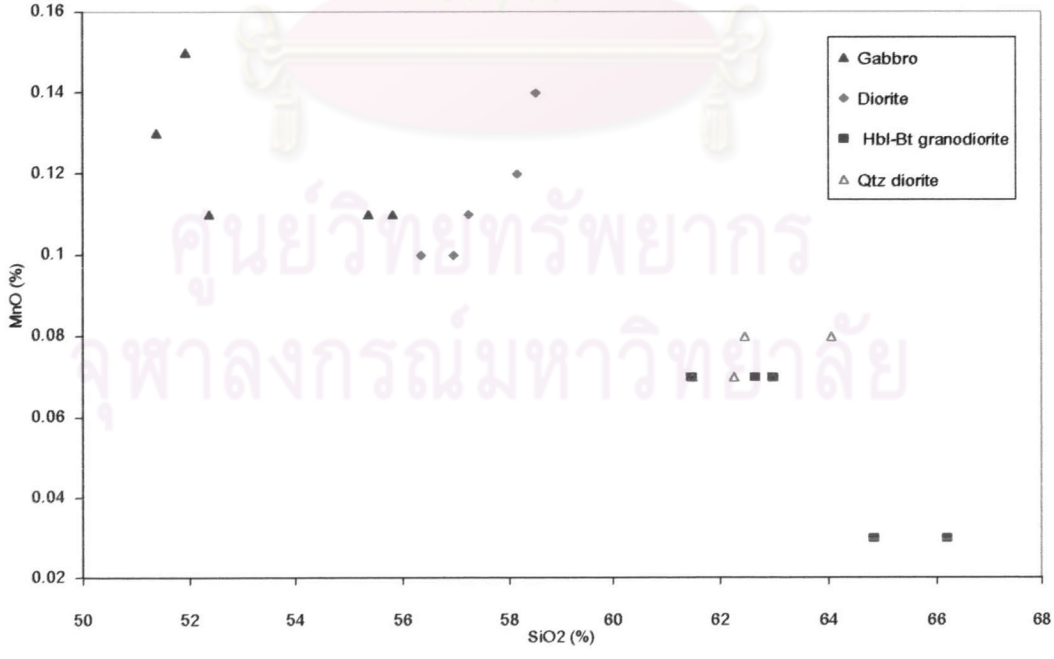

Figure 4.14 Harker variation diagram shows a decreasing of MnO with respect to increasing of SiO_2 content.

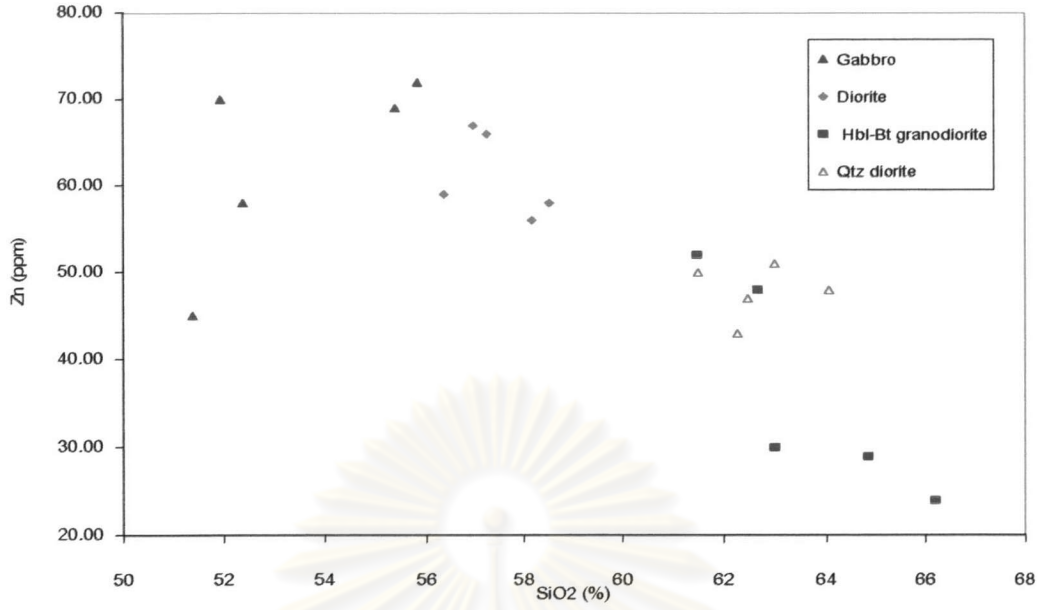

Figure 4.15 Harker variation diagram shows a decreasing of Zn with respect to increasing of SiO_2 content.

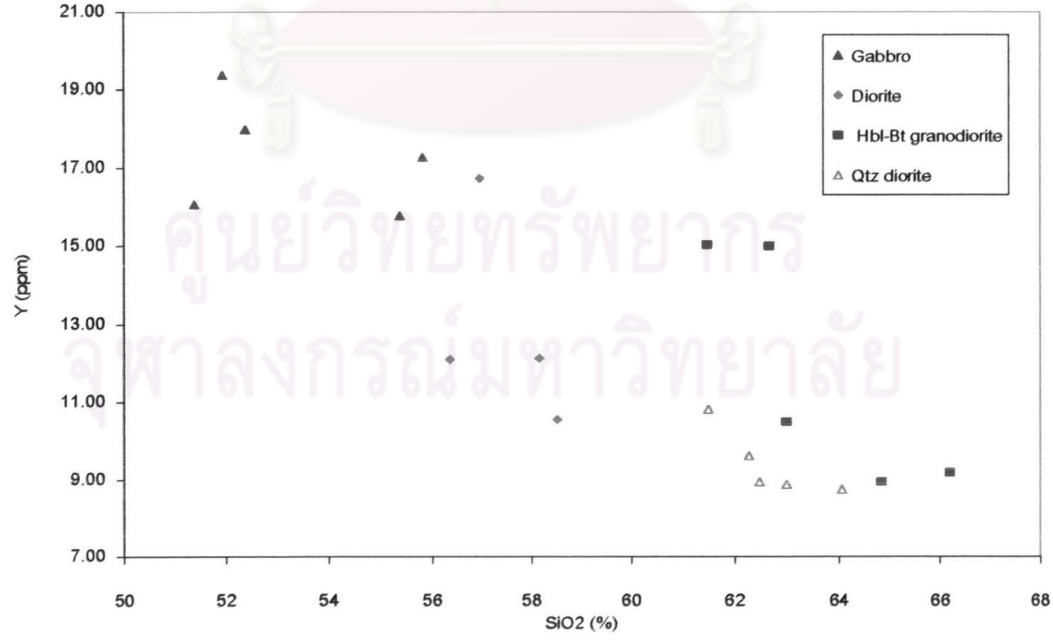

Figure 4.16 Harker variation diagram shows a decreasing of Y with respect to increasing of SiO_2 content.

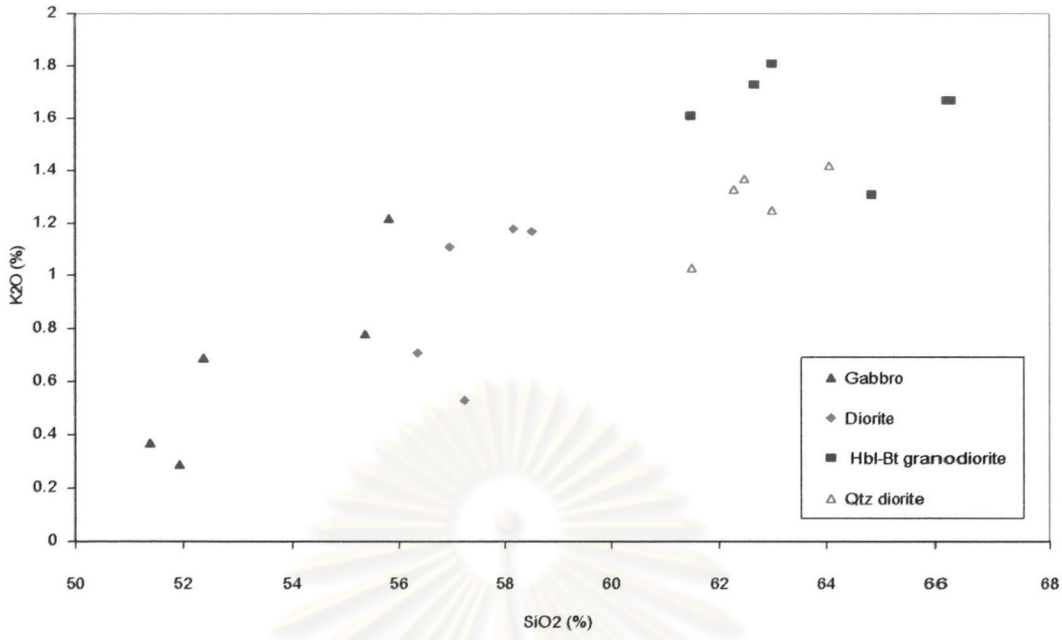

Figure 4.17 Harker variation diagram shows a increasing of K_2O with respect to increasing of SiO_2 content.

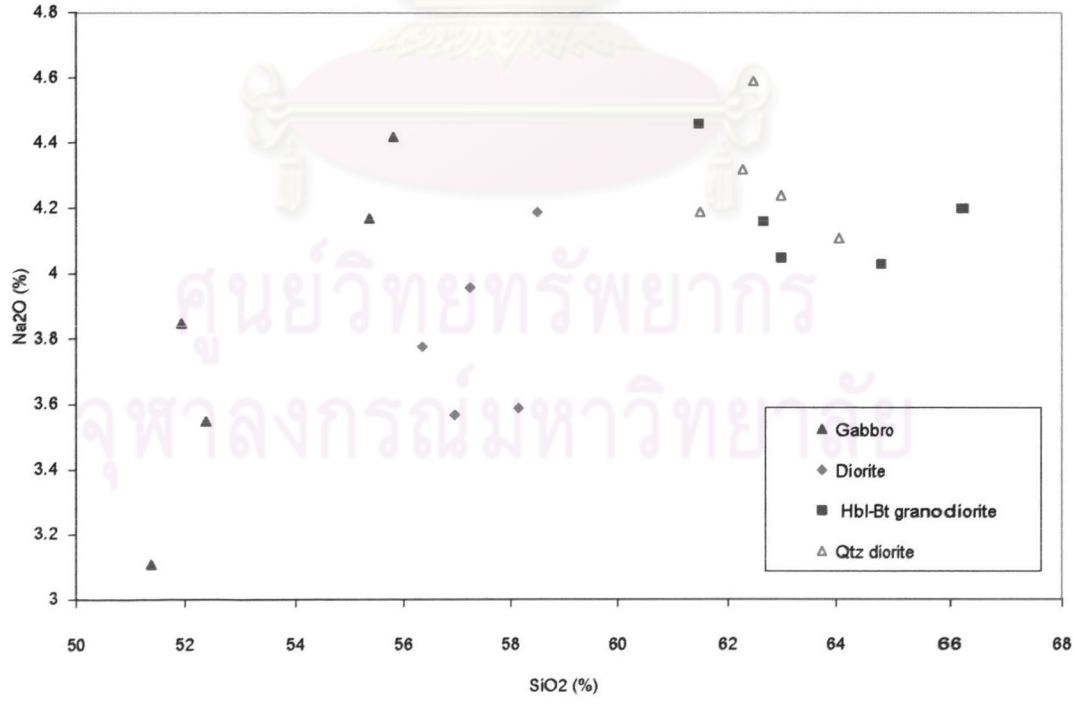

Figure 4.18 Harker variation diagram shows a increasing of Na_2O with respect to increasing of SiO_2 content.

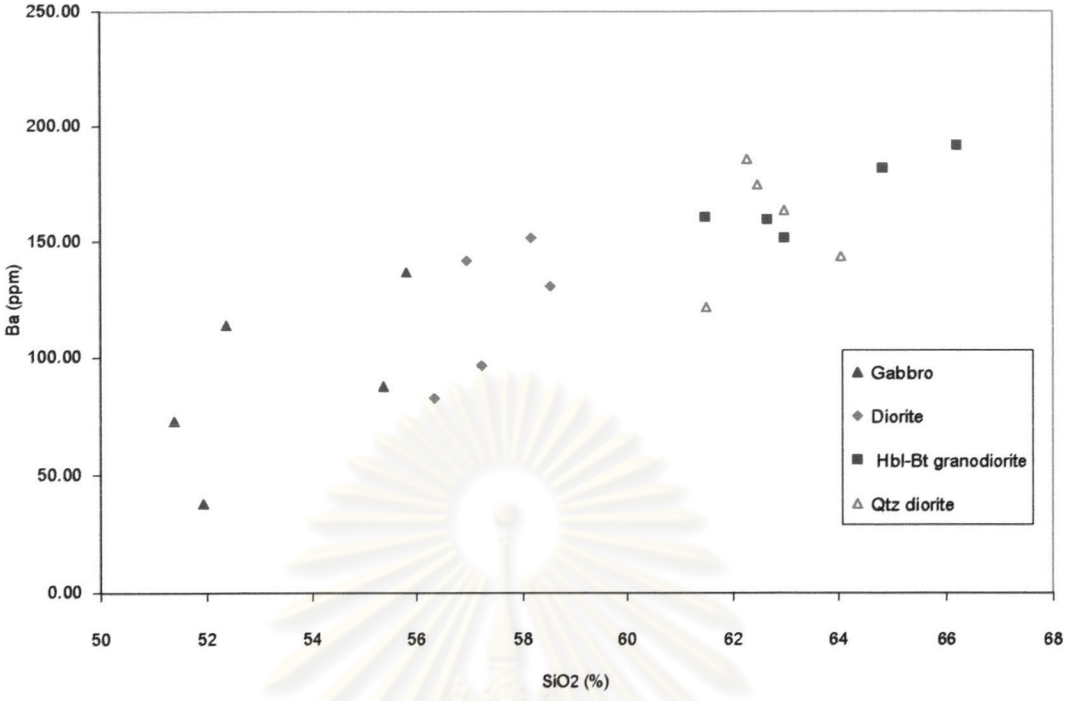

Figure 4.19 Harker variation diagram shows a increasing of Ba with respect to increasing of SiO_2 content.

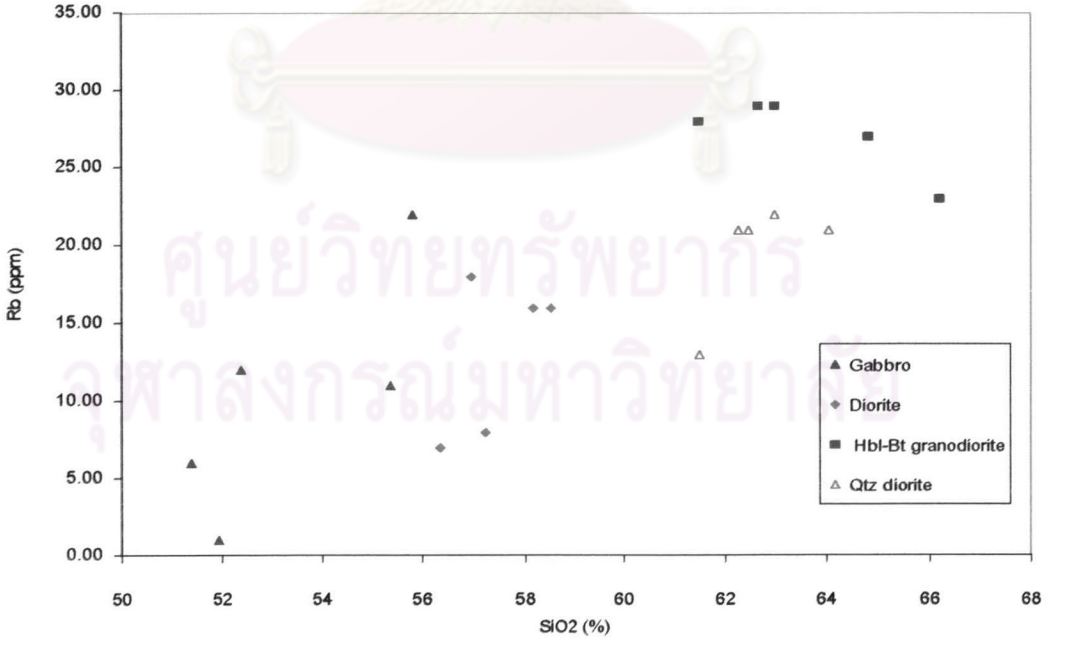

Figure 4.20 Harker variation diagram shows a increasing of Rb with respect to increasing of SiO_2 content.

4.2.5 Chemical Affinity

The plot of Na_2O versus K_2O contents shows that the four intrusive rocks in the study area have the chemical characteristic of I-Type after Chappell and White (1974) as shown in Figure 4.21. Moreover, their aluminum saturated index, molar of $Al_2O/(CaO+Na_2+K_2O)$, in Table 4.2 suggest metaluminous with subordinate peraluminous types. The plot of K_2O versus SiO_2 contents shows that the four intrusive rocks in the study area fall in the calc-alkaline series in which the hornblende-biotite granodiorite is more toward the high K-calc-alkaline series (Figure 4.22).

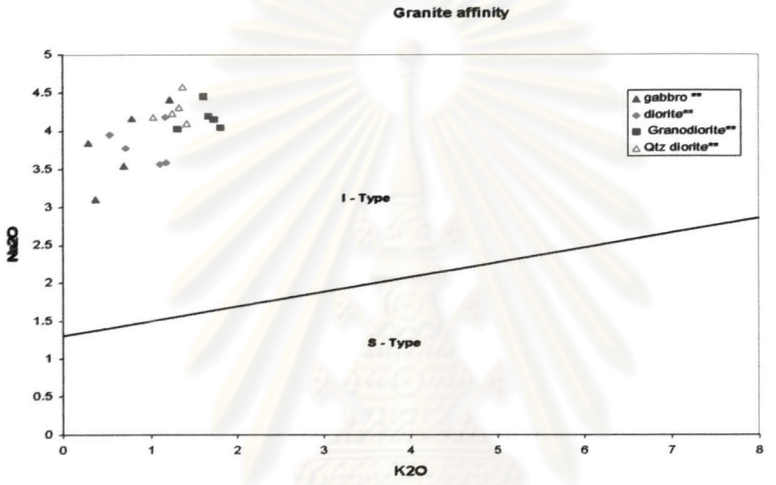

Figure 4.21 Na_2O vs K_2O diagram represents the affinity of intrusive rocks in study area (after Chappell and White, 1974).

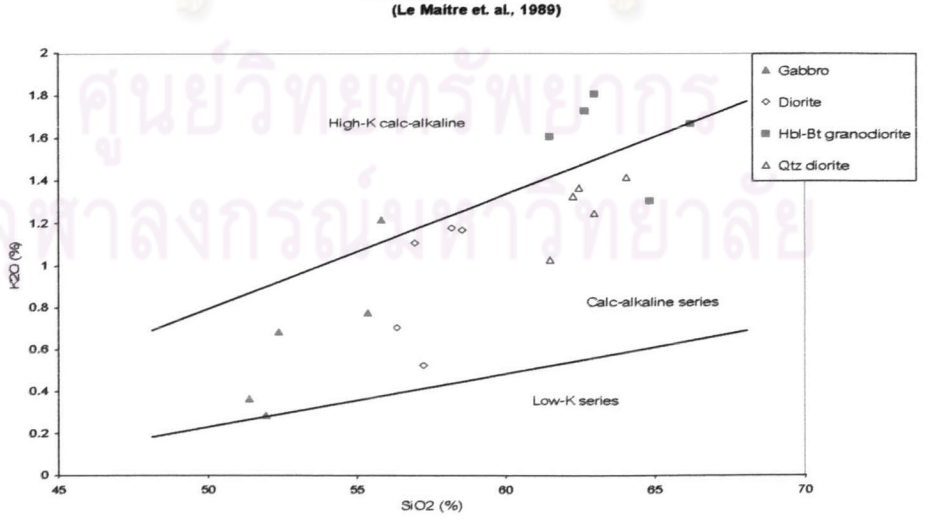

Figure 4.22 Subalkalic subdivision of intrusive rocks in the study area.

Table 4.2 Summary of aluminum saturated index.

	Gabbro					Diorite				
Major elements	pn 65	pn 66	pn 68	pn 69	pn 70	pn 22	pn 30	pn 44	pn 50	pn 54
Al2O3	17.03	18.3	16.05	17.49	17.15	17.18	16.49	17	16.74	17.58
CaO	7.81	14.32	12.55	10.71	6.78	6.91	8.7	7.25	6.2	7.03
Na2O	4.17	3.11	3.85	3.55	4.42	3.59	3.78	3.57	4.19	3.96
K2O	0.78	0.37	0.29	0.69	1.22	1.18	0.71	1.11	1.17	0.53
mole of Al2O3/(CaO+Na2O + K2O)	0.78	0.58	0.54	0.67	0.82	0.87	0.72	0.84	0.86	0.88
mole of Al2O3/(Na2O + K2O)	2.21	3.32	2.41	2.66	2.00	2.39	2.36	2.40	2.05	2.48
	Metaluminous	Metaluminous	Metaluminous	Metaluminous	Metaluminous	Metaluminous	Metaluminous	Metaluminous	Metaluminous	Metaluminous
	Hbl-Bt granodiorite					Qtz diorite				
Major elements	pn 36	pn 37	pn 38	pn 58	pn 59	pn 2	pn 4	pn 6	pn 7	pn 20
Al2O3	16.04	16.78	15.39	16.11	16.11	15.46	15.21	17.38	15.87	17.51
CaO	3.74	5.17	3.44	5.29	5.31	4.49	5.94	4.54	4.3	5.3
Na2O	4.2	4.05	4.03	4.46	4.16	4.32	4.59	4.11	4.24	4.19
K2O	1.67	1.81	1.31	1.61	1.73	1.33	1.37	1.42	1.25	1.03
mole of Al2O3/(CaO+Na2O + K2O)	1.03	0.93	1.08	0.86	0.88	0.93	0.77	1.05	0.98	0.99
mole of Al2O3/(Na2O + K2O)	1.84	1.95	1.91	1.77	1.85	1.81	1.68	2.09	1.91	2.19
	Peraluminous	Metaluminous	Peraluminous	Metaluminous	Metaluminous	Metaluminous	Metaluminous	Peraluminous	Metaluminous	Metaluminous

4.2.6 Signatures of trace and rare earth elements

Tectonic discrimination diagrams (Figures 4.23 and 4.24) indicate that all intrusive rocks in the study area are classified as volcanic-arc granitic rock (VAG) after Pearce et al., 1984. However, some data points of diorite and gabbro fall around the boundary of VAG and within-plate granite (WPG). As discussed by Pearce et al. (1984), those samples which fall in the fields of WPG and oceanic-ridge granite (ORG) may be affected by the presence of clinopyroxene and hornblende which are preferred to accumulate the compatible elements, such as Nb and Y.

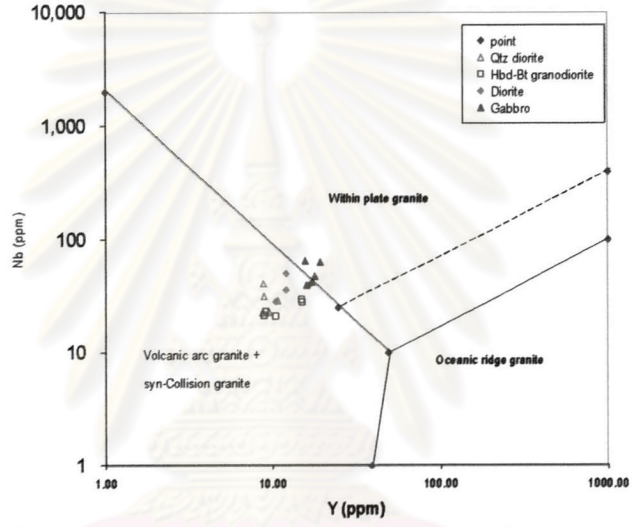

Figure 4.23 The Nb-Y discrimination diagram for granitic rocks (after Pearce et al., 1984).

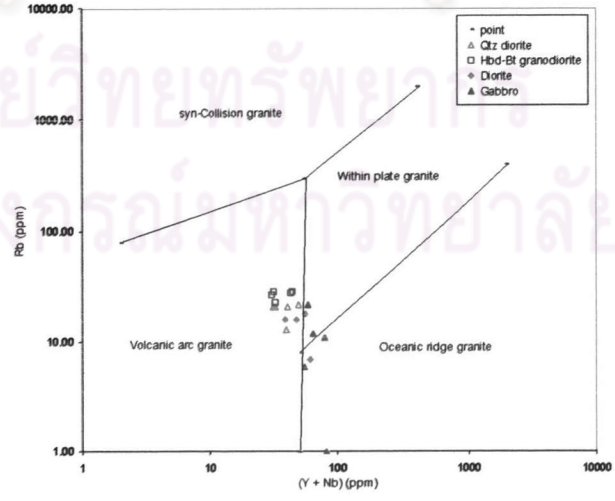

Figure 4.24 The Rb-(Y+Nb) discrimination diagram for granitic rocks (after Pearce et al., 1984).

In the mineral vector diagram which was established from the partitioning coefficient of Ba and Sr in magmatic system, the content of these elements in magmatic system will be changed by a fractionation of the mineral assemblage, such as plagioclase, clinopyroxene, orthopyroxene, hornblende, biotite and K-feldspar (Rollinson, 1993). The plot of such elements in the diagram (Figure 4.25) reveal that the fractionation of clinopyroxene and plagioclase are the main cause of chemical variation among the four intrusive rocks in the study area.

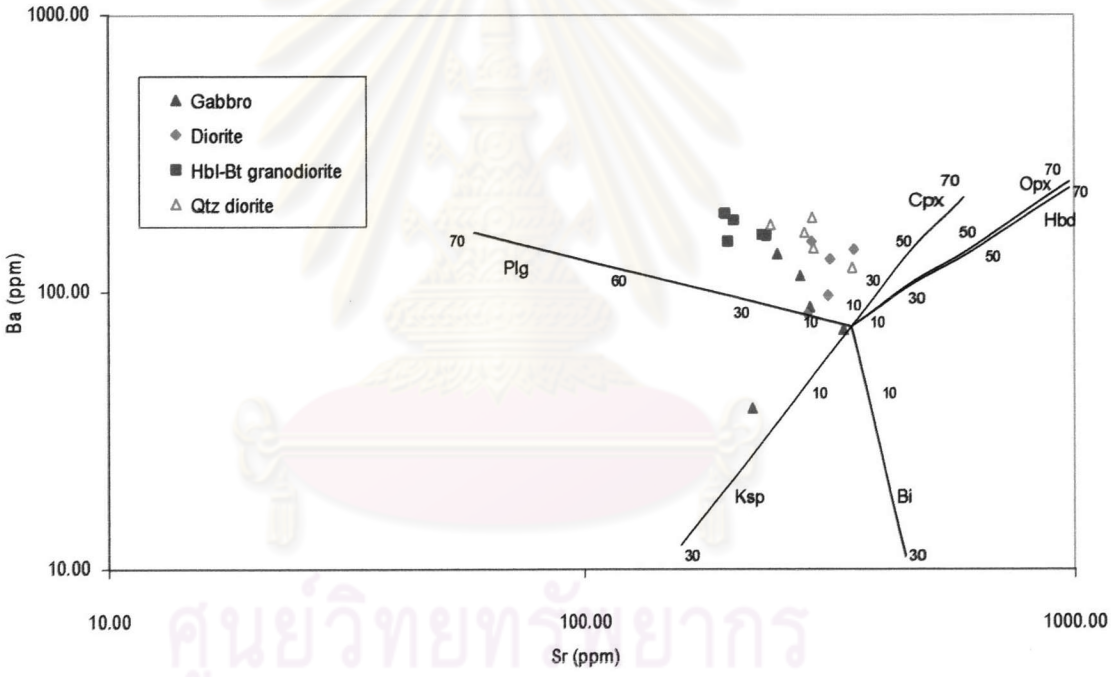

Figure 4.25 Mineral vector diagram shows the effects of clinopyroxene and plagioclase on the variation among intrusive rocks in the study area (after Rollinson, 1993).

Rare earth concentration of rock samples are normalized to chondrite referent values from Nakamura (1974). The vector diagram (Figure 4.26) shows the changes in normalized (Ce/Sm) versus Ce concentration during the partial melting of a primitive mantle source applied to the four intrusive rock types in study area and compared with extrusive rocks from Intasopa (1993). The plot results are close to the path way of fractional melting with 2 to 5 % degree of melting.

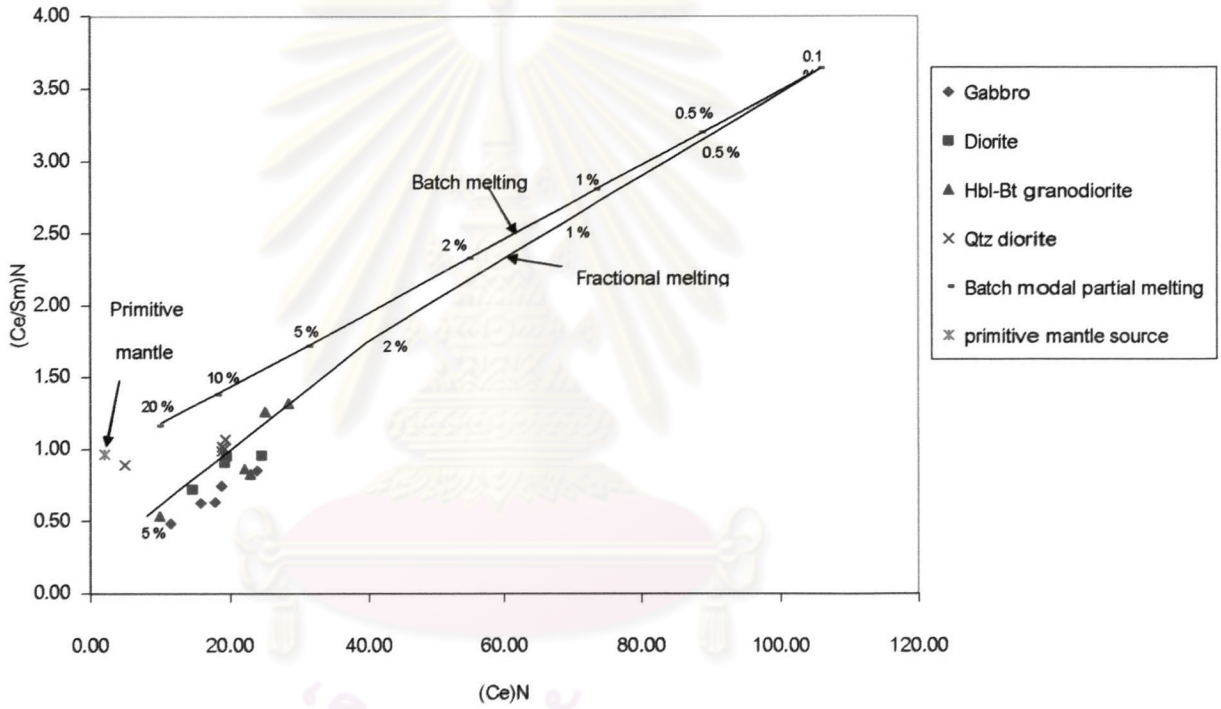

Figure 4.26 Vector diagram shows the changes in normalized (Ce/Sm) versus Ce concentration during the partial melting of a primitive mantle source applied to four intrusive rock types in study area and compared with extrusive rocks form Intasopa (1993).

The spider diagrams or chondrite-normalized rare earth patterns of each rock type are shown in Figures 4.27 to 4.31. These REE patterns of the whole rock samples show the following features:

1. All the intrusive rocks are enriched in REE relative to chondrite and have the same pattern, nearly parallel to each other.
2. All of them are enriched in LREE and MREE with slightly negative Eu-anomaly.
3. The more felsic hornblende-biotite granodiorite and quartz diorite have relatively high abundance in LREE, La_N and Ce_N, but low MREE and HREE as compared with those of the more mafic pyroxene diorite and diorite.
4. In contrast, the two more mafic rocks have higher abundance of MREE and HREE than those of the two more felsic rocks.
5. All the rocks have REE abundance fall in the field of andesite of Phetchabun carried out by Intasopa (1993), although they have more deviation.
6. Hornblende-biotite granodiorite has the most deviated pattern within its group which may suggest the variation within the pluton.

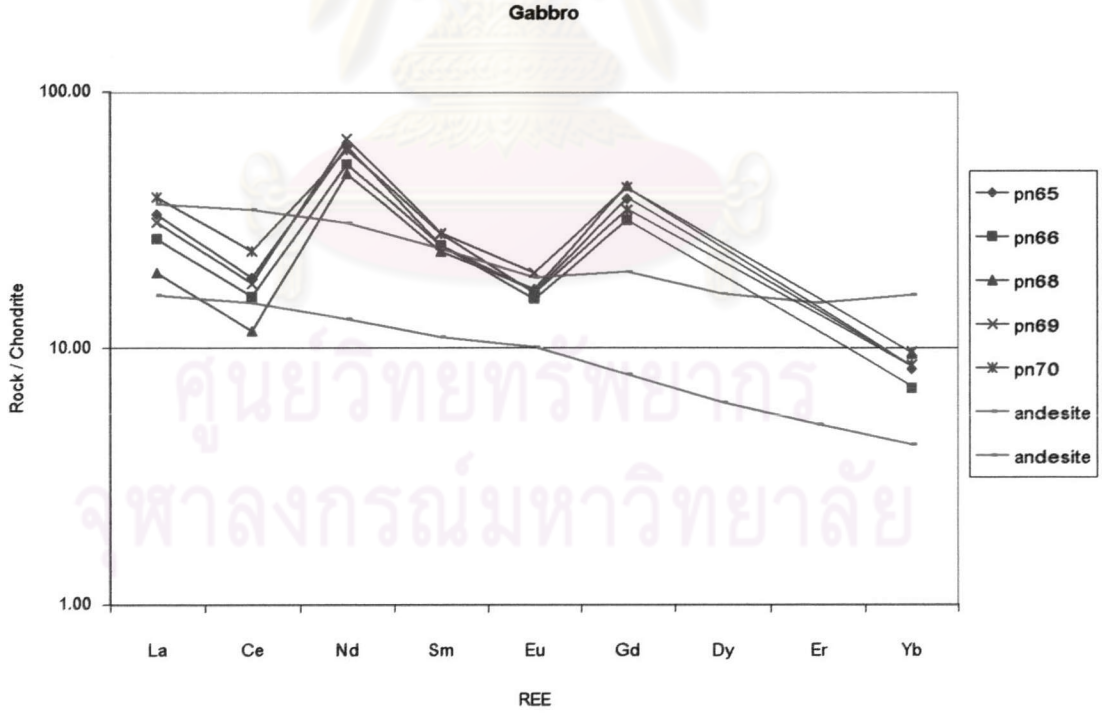

Figure 4.27 Chondrite-normalized rare earth pattern of the gabbro compare to each others and andesite of adjacent area (data from Intasopa, 1993).

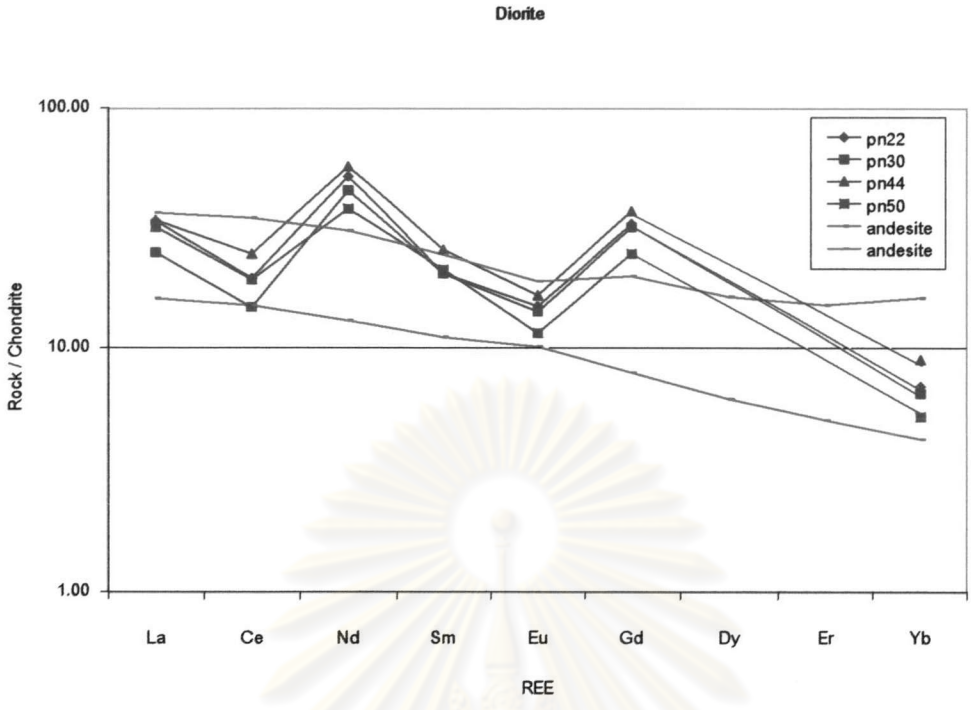

Figure 4.28 Chondrite-normalized rare earth pattern of the diorite compare to each others and andesite of adjacent area (data from Intasopa, 1993).

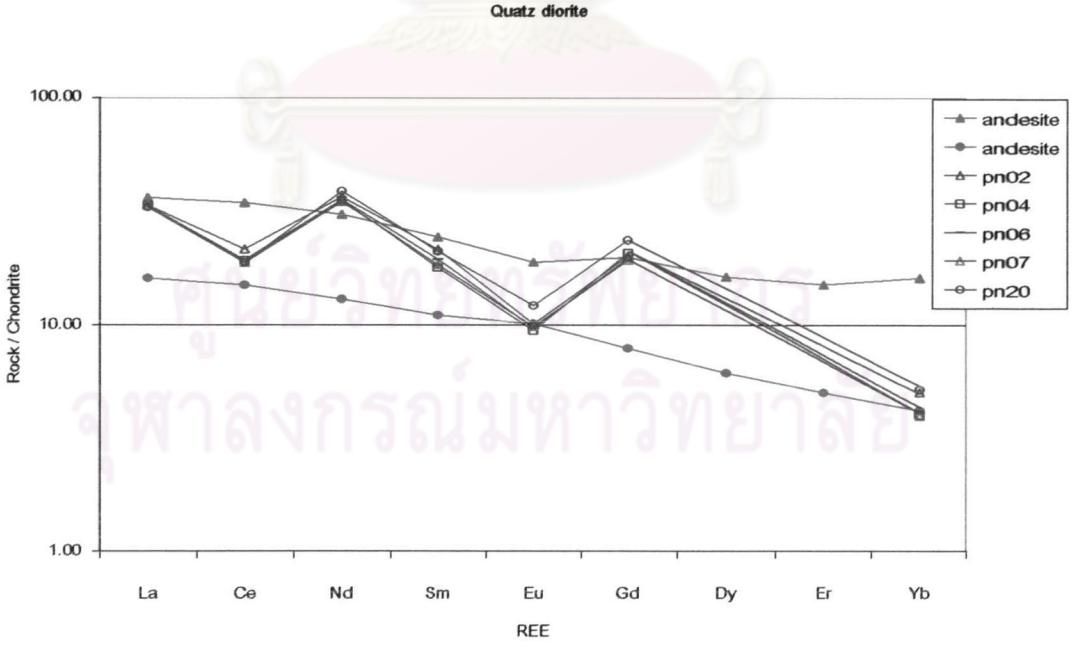

Figure 4.29 Chondrite-normalized rare earth pattern of the quartz diorite compare to each others and andesite of adjacent area (data from Intasopa, 1993).

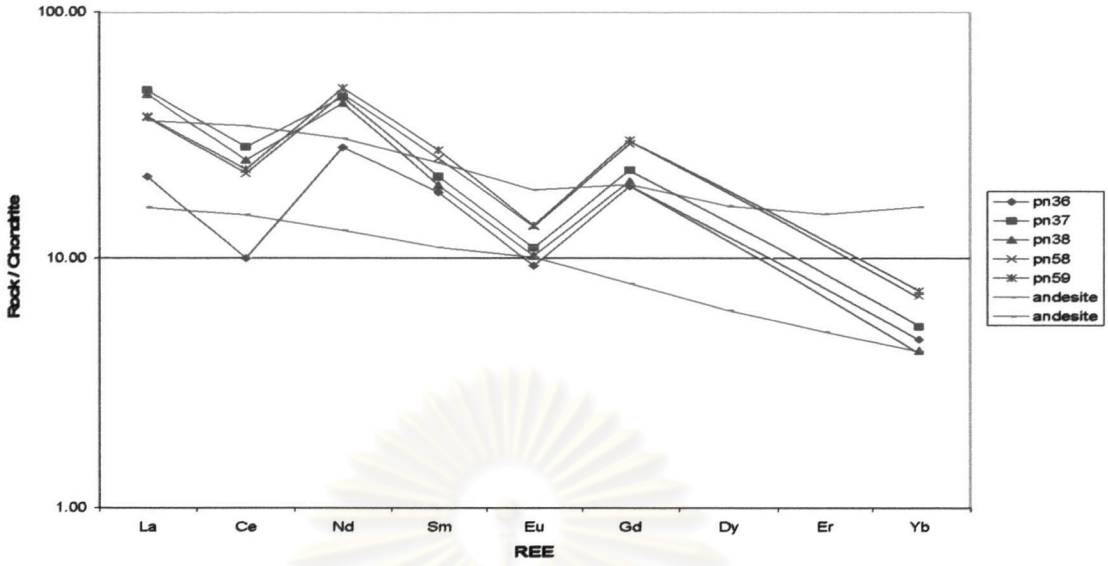

Figure 4.30 Chondrite-normalized rare earth pattern of the hornblende-biotite granodiorite compare to each others and andesite of adjacent area (data from Intasopa, 1993).

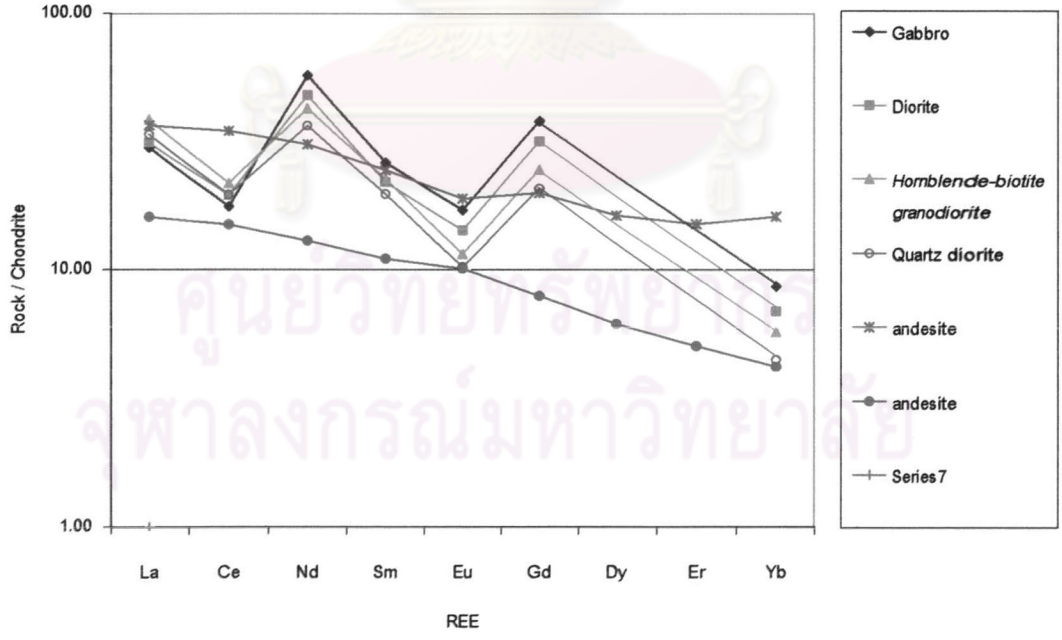

Figure 4.31 Chondrite-normalized rare earth pattern of the intrusive rocks in the study area compare to each others and andesite of adjacent area (data from Intasopa, 1993).

4.3 Mineral chemistry

The Al^{total} contents in hornblende which determined by EPMA were used for pressures calculation in a spreadsheet using the equation of Schmidt (1992),

$$P (\pm 0.6 \text{ kbar}) = -3.01 + 4.76\, Al^{tot} \quad \text{.....(1)}$$

where Al^{tot} is the amount of total aluminum in hornblende on the basis of 23 oxygen.

Temperature is calculated from the non-ideal model using activities of both amphibole and plagioclase after Holland and Blundy (1994), called 'amphibole-plagioclase thermometer'. The mole fractions of albite in plagioclase and Al-content in hornblende were taken from the EPMA results in Appendix D-1 and D-3. The amphibole-plagioclase thermometer is based on the following reaction:

$$\underset{\text{edenite}}{NaCa_2Mg_5Si_4(AlSi_3)O_{22}(OH)_2} + 4SiO_2 \;(\text{quartz}) = \underset{\text{tremolite}}{Ca_2Mg_5Si_8O_{22}(OH)_2} + \underset{\text{albite}}{NaALSi_3O_8}$$

The edenite –tremolite thermometer assemblaged with quartz is

$$T_A = \frac{(-76.95+0.79P+Y_{ab}+39.4\,X^A_{Na}+22.4X^A_K+(41.5-2.89P)*X^{M2}_{Al})}{-0.0650-R*\ln((27*X^A_{\#}*X^{T1}_{Si}*X^{plag}_{ab}) / (256*X^A_{Na}*X^{T1}_{Al}))} \quad \text{.....(2)}$$

where Y_{ab} term = 0, if $X_{ab}>0.5$

or $Y_{ab} = 12.0(1-X_{ab})^2-3.0$ kJ, if $X_{ab}<0.5$

$X^A_{Na} = Ca+Na+cm-2$, $X^A_K = K$

$X^{M2}_{Al} = (Al+Si-8)/2$, $X^A_{\#} = 3-Ca-Na-cm$

$X^{plag}_{ab} = Na/(Ca+Na+K)$, $X^{T1}_{Al} = (8-Si)/4$

$Cm = Si+Al+Ti+Fe^{3+}+Fe^{2+}+Mg+Mn-13.0$

The calculated pressure and temperature of emplacement of intrusive rocks in the study area are summarized in Table 4.3 below.

Table 4.3 Summary of calculated P –T of emplacement of the three rock types in the study area.

Rock	Pressure Range (kbar)	SD (Pressure kbar)	Average Temperature (^{0}C)	SD (Temperature ^{0}C)
Gabbro	2.6 – 2.7	0.1	627	-
Diorite	4.6 – 6.6	0.74	452	-
Quartz diorite	2.5 – 2.8	0.25	609	1.17
Hbd-Bi granodiorite	0.7 – 1.0	0.38	671	19

Based on the fact that those four intrusive are closely related spatially and might have the same genetic link. As will be discussed later, these intrusive rocks might also relate closely to the volcanic rocks in the study area both spatially and temporally. These facts may suggest that those four intrusive rocks were intruded to a high level or sub-volcanic level by which both intrusive and extrusive rocks were found together. Hence the pressures and probably temperatures of crystallization of those four intrusive rocks should not have significantly different. However, the calculated results of both pressure and temperature show inconsistent values. For examples, diorite yields too high pressure and too low temperature and hornblende-biotite granodiorite yields too low pressure. These inconsistent values may be due to either error of analysis or some alteration processes. Therefore the pressure and temperature of diorite will be ignored for the discussion, while the pressure of hornblende-biotite granodiorite will be discussed below.

In case of pressure which calculated from the content of total aluminum in hornblende, based on the theory, the capability of Al in the tschermak substitution, Al replaces for Mg at M_2 and Si at T_1 crystallographic site, will increase when the pressure

increases. Speer (1987; in Pitcher, 1997) found that hornblende would loss its Al content if it was replaced by biotite. The petrographic study reveals that hornblende in hornblende-biotite granodiorite is usually replaced by biotite. Therefore its Al content might decrease which then yields an anomalously low pressure. As a result, the pressure calculated for hornblende-biotite granodorite may be too low to give a reasonable value.

By ignoring the anormalously high and low pressure and temperature values. The most probably ranges of pressure and temperature for those four intrusive rocks are 2.5 to 2.8 kbar, and 609 to 671°C, respectively. The slight temperature variation found among the four intrusive rocks may be due to the activity of volatiles because Johnson and Rutherford (1989) found that the presence of mixed CO_2-H_2O in magmatic system will achieve high solidus temperature. The role of this factor is clearly observed in hornblende-biotite granodiorite which yields the highest temperature value. The hornblende-biotite granodiorite is the most felsic therefore it tends to cumulate more volatile. This result may relate to the field evidence that there is a large body of iron skarn in limestone that contact with the hornblende-biotite granodiorite at the south-western part of the study area.

4.4 Geochronology

Two grains of zircon from a polished thin section of gabbro (Figure 4.32) were analyzed of the isotopic compositions by LA-ICP MS and the isotopic ratios and the external standard materials are given in Table 4.4. The Pb206/U238 and Pb207/U235 ratios of the samples are plotted in the concordia diagram (Figure 4.32) which yields 230 ± 4 Ma.

Table 4.4 isotopic ratios of samples and standard materials
(samples include A13A-1, A13-A-2, A13C-1 and A13C-2)

Samples & Standard	Pb206/U238	Pb207/U235
GJ-1(external std)	0.09744	0.80984
GJ-2(external std)	0.09796	0.80976
MT-1(external std)	0.11456	1.03314
91500-1(external std)	0.17491	1.7945
MT-2 (external std)	0.11377	0.99765
GJ-3(external std)	0.09726	0.80865
A13A-1	**0.03785**	**0.27969**
A13A-2	**0.03947**	**0.3867**
A13C-1	**0.03779**	**0.27193**
A13C-2	**0.03878**	**0.28586**
GJ-4(external std)	0.09802	0.81421
GJ-5(external std)	0.09734	0.80759

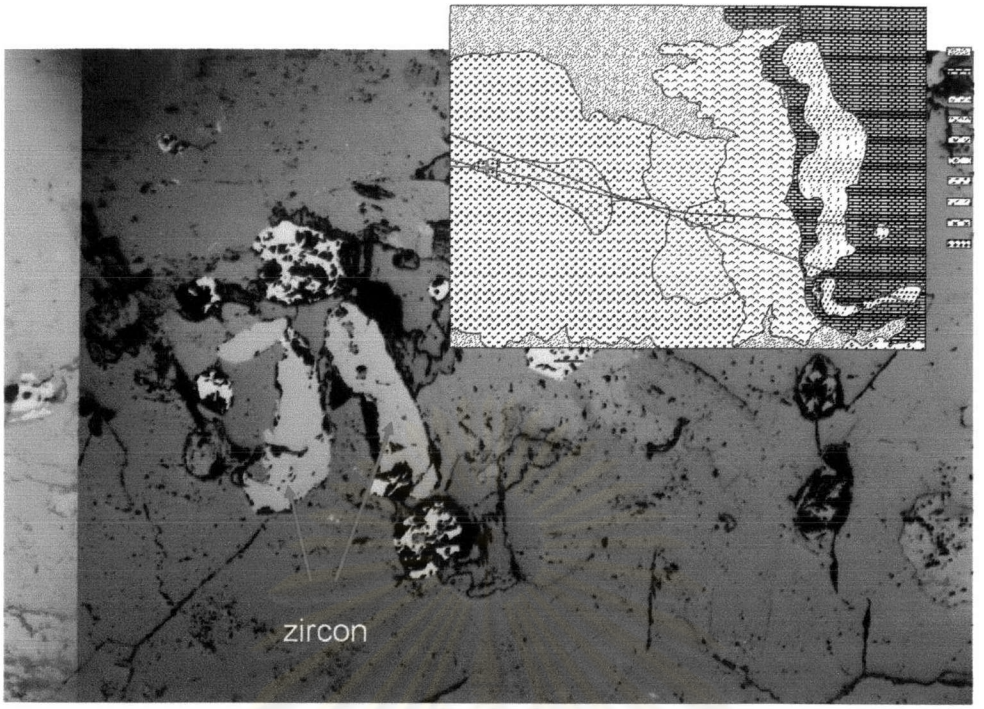

Figure 4.32 Two zircon crystals for U-Pb dating by LA-ICP MS

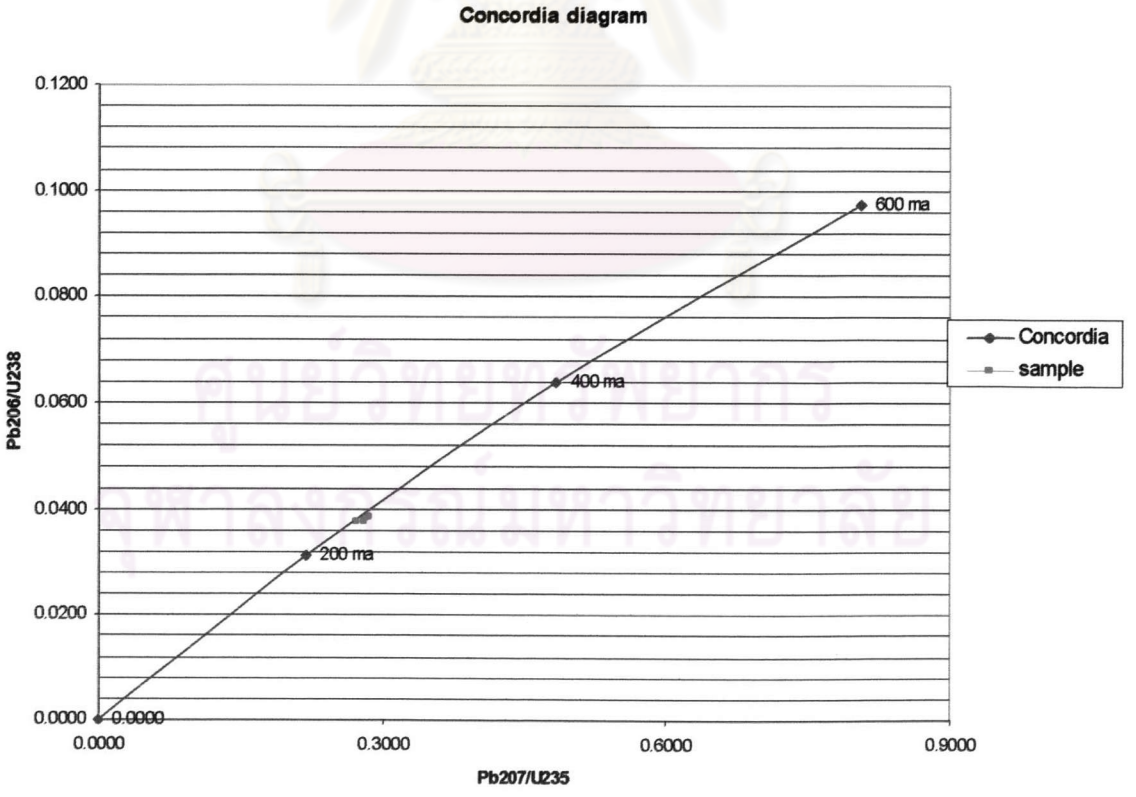

Figure 4.33 showing the plot of in situ zircon dating values in the Concordia.

The U-Pb age from *in situ* zircon dating by LA-ICP-MS suggests that the gabbro might emplace during middle Triassic (230 ± 4 Ma). The volcanic rocks which had been dated by Intasopa (1993) using the $^{40}Ar/^{39}Ar$ method (from hornblende) yielded 238 ± 4 and 237 ± 12 Ma for basaltic andesite and andesite, respectively. This evidences suggest that the intrusive rocks, at least the gabbro, might be somewhat slightly younger (even though those dated ages are within their error bars) than the volcanic rocks in the study area. This assumption can be supported by field relationship, such as the gabbro crosscutting pyroclastic rocks, hornblende-biotite granodiorite crosscutting andesite and basalt, and the presence of basalt xenoliths in quartz diorite. Because of the dated ages of both intrusive and extrusive igneous rocks are very close to one another. They were therefore closely related to each other spatially and temporally.